journal of the mechanical behavior of biomedical materials 150 (2024) 106259

Contents lists available at ScienceDirect

Journal of the Mechanical Behavior of Biomedical Materials

journal homepage: www.elsevier.com/locate/jmbbm

The 2-layer elasto-visco-plastic rheological model for the material parameter identification of bone tissue extended by a damage law

Andreas G. Reisinger [a,b,*], Martin Bittner-Frank [a,b], Philipp J. Thurner [b], Dieter H. Pahr [a,b]

[a] Department of Anatomy and Biomechanics, Karl Landsteiner University of Health Sciences, Austria
[b] Institute of Lightweight Design and Structural Biomechanics, Vienna University of Technology, Austria

ARTICLE INFO

Keywords:
2-layer rheological model
Damage
Trabecular bone
Single trabecula
Plasticity
Viscosity
Material parameter identification
Optimization

ABSTRACT

The response of bone tissue to mechanical load is complex and includes plastic hardening, viscosity and damage. The quantification of these effects plays a mayor role in bone research and in biomechanical clinical trials as to better understand related diseases.

In this study, the damage growth in individual wet human trabeculae subjected to cyclic overloading is quantified by inverse rheological modeling.

Therefore, an already published rheological material model, that includes linear elasticity, plasticity and viscosity is extended by a damage law. The model is utilized in an optimization process to identify the corresponding material parameters and damage growth in single human trabeculae under tensile load.

Results show that the damage model is leading to a better fit of the test data with an average root-mean-square-error (RMSE) of 2.52 MPa compared to the non-damage model with a RMSE of 3.03 MPa. Although this improvement is not significant, the damage model qualitatively better represents the data as it accounts for the visible stiffness reduction along the load history. It returns realistic stiffness values of 11.92 GPa for the instantaneous modulus and 5.73 GPa for the long term modulus of wet trabecular human bone. Further, the growth of damage in the tissue along the load history is substantial, with values above 0.8 close to failure. The relative loss of stiffness per cycle is in good agreement with comparable literature.

Inverse rheological modeling proves to be a valuable tool for quantifying complex constitutive behavior from a single mechanical measurement. The evolution of damage in the tissue can be identified continuously over the load history and separated from other effects.

1. Introduction

Mechanical testing is the gold standard for investigating the material response of biological tissues and of bone in particular. It results in a set of stress–strain data, from which material property values are extracted. The constitutive behavior of bone tissue is complex, as it exhibits plastic hardening, viscosity and damage as the most prominent effects besides linear elasticity, (Reilly et al., 1974; McElhaney, 1966; Fondrk et al., 1988; Keaveny et al., 1994b). Depending on the utilized loading protocol, mechanical test data include a mixture of the mentioned effects, making it hard to quantify their individual contributions. The Young's modulus is usually determined by the slope of a supposedly initial linear region. Different methods exist for finding the yield limit, which very likely return different values for the same data, (Synek et al., 2015; Keaveny et al., 1994a; Reilly and Burstein, 1975). This is problematic for an intrinsic material property. Damage is associated with the degradation of stiffness, (Carter and Hayes, 1977b,a), and identified by extracting the tangent stiffness of successive load cycles with increasing amplitude. Viscosity is investigated by cyclic, relaxation or creep tests and is obscuring the Young's modulus and yield stress as both quantities depend on loading rate, (McElhaney, 1966; Lakes et al., 1979; Sasaki et al., 1993).

A simultaneous determination of all those effects from a single specimen is difficult but can be attempted by using a mathematical material model in an inverse approach on a stress–strain dataset obtained from a suitable loading protocol, (Muller and Hartmann, 1989; Ichikawa and Ohkami, 1992; Gelin and Ghouati, 1995). Hereby, the material parameters of the model are optimized so that the stress–strain output of the model matches best the stress–strain data of the experiment. It is supposed that the found parameters characterize the specimens material properties. In this approach, the material model needs to exhibit the constitutive effects of the material that is investigated.

* Corresponding author at: Department of Anatomy and Biomechanics, Karl Landsteiner University of Health Sciences, Austria.
E-mail address: andreas.reisinger@kl.ac.at (A.G. Reisinger).

https://doi.org/10.1016/j.jmbbm.2023.106259
Received 27 June 2023; Received in revised form 24 October 2023; Accepted 16 November 2023
Available online 18 November 2023

On the level of sub-millimeter bone structural units like trabeculae, the above-mentioned elastic, plastic and viscous effects, need to be included when performing cyclic overloading. There is ongoing investigation at which length-scale the effect of damage is kicking in. It was shown in Schwiedrzik et al. (2014) that for lamellar bone specimens as small as ~5 μm no stiffness degradation i.e. damage can be observed. On the level of individual trabeculae (diameter ~ 100 μm) or small cortical bone samples of comparable size, overloading produces microcracks with crack bridging fibrils or diffuse damage (Zioupos, 1999; Nalla et al., 2003; Thurner et al., 2007; Szabó et al., 2011; Vashishth et al., 2000). The damaged zones clearly appear as whitening and cyclic experiments reveal a degradation of stiffness for bone specimens at that length-scale, e.g. Frank et al. (2021). The growth of damage along the load history is hard to determine, as signal noise and viscous hysteresis is obscuring the data. Inclusion of damage into an inversely applied rheological model, allows separation of damage growth from other constitutive effects.

Plenty material models for bone tissue exist that incorporate plastic, viscous and damage properties in different combinations, (Garcia, 2006; Garcia et al., 2010; Schwiedrzik et al., 2014; Schwiedrzik, 2014; Natali et al., 2008; Fondrk et al., 1999; Mirzaali et al., 2015). Consequently, there is a gap in knowledge the characterization of the true trabecular bone material properties. Such characterization should include all known constitutive effects. Providing an approach to extract and separate all constitutive effects, would allow to determine pathological and age-related changes in the mechanical competence of bone tissue. This is an unmet need for bone diseases such as osteoporosis.

In this study, we extend the 2-layer elasto-visco-plastic rheological model from Reisinger et al. (2020) by a damage law to better reproduce the uniaxial behavior of small length-scale bone samples and to quantify the growth of damage in the tissue. The new model and its predecessor are used for the material parameter identification of the same set of individual human bone trabeculae, that were tested experimentally in wet condition. Stiffness, damping, yield stress and hardening coefficients of the trabeculae are determined by both models and compared. The growth of damage along the load history is quantified and discussed.

2. Methods

2.1. The 2-layer elasto-visco-plastic-damage rheological model

Bone's response to mechanical load includes different energy dissipation mechanisms. Beyond the yield point, bone is exhibiting plastic flow, (Reilly et al., 1974), and damage, (Zioupos and Currey, 1994). In addition, its mechanical behavior is depending on strain rate and thus contains a viscous contribution, (McElhaney, 1966).

The 2-layer rheological model described in the following is an update to the model published recently in Reisinger et al. (2020). In this new version, it aims to capture also the damage behavior of single bone trabeculae under cyclic tensile load beside their plastic and viscous response.

The 2-layer rheological model consists of a Prandtl model and a Maxwell model arranged as two parallel layers as illustrated in Fig. 1. The total model stress σ_{mod} is the sum of the stress σ_{pr} in the Prandtl layer and the stress σ_{mx} in the Maxwell layer.

$$\sigma_{\mathrm{mod}} = \sigma_{\mathrm{pr}} + \sigma_{\mathrm{mx}} \tag{1}$$

and in terms of stress rates,

$$\dot{\sigma}_{\mathrm{mod}} = \dot{\sigma}_{\mathrm{pr}} + \dot{\sigma}_{\mathrm{mx}} \tag{2}$$

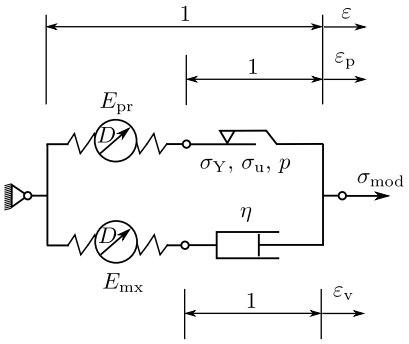

Fig. 1. Two Layer Rheological Model, consisting of a Prandtl layer and a Maxwell layer in parallel with the associated layer stresses σ_{pr} and σ_{mx}, respectively. The strain in the plastic slider is denoted as ε_{p} and the strain in the damper as ε_{v}. E_{pr}, E_{mx} are the *initial* elastic moduli of the springs. The springs degrade in stiffness based on a damage scalar D. σ_{Y}, σ_{u} are yield- and ultimate stress, p is the exponential hardening exponent and η the damping parameter. The model's global state is described by the global stress σ_{mod} and global strain ε.

Prandtl layer:. The Prandtl layer itself is built from an elastic spring with initial elastic modulus E_{pr} in series with a plastic slider, (Sperry, 1964; Grzesikiewicz and Zbiciak, 2012). The stiffness of the elastic spring is degrading from its initial value E_{pr} in the amount of damage D that monotonically increases between $0 \leq D \leq 1$ resulting in a degraded elastic modulus $\hat{E}_{\mathrm{pr}}$ given by

$$\hat{E}_{\mathrm{pr}} = (1 - D)E_{\mathrm{pr}} \tag{3}$$

In the Prandtl layer, the total strain ε of the two-layer model splits into an elastic part and a plastic part ε_{p} resulting in the elastic relationship

$$\sigma_{\mathrm{pr}} = \hat{E}_{\mathrm{pr}}(\varepsilon - \varepsilon_{\mathrm{p}}) \tag{4}$$

For the plastic slider, a yield condition f is defined whose yield limit is expanding exponentially in the amount of equivalent plastic strain α, see also Voce (1948), Garcia et al. (2010), Schwiedrzik et al. (2014), which was also shown to represent the characteristics of bone hardening in Carretta et al. (2013a), Reisinger et al. (2020) very well.

$$f(\sigma_{\mathrm{pr}}, \alpha) = |\sigma_{\mathrm{pr}}| - [\sigma_{\mathrm{Y}} + (\sigma_{\mathrm{u}} - \sigma_{\mathrm{Y}})(1 - \exp(-\alpha p))] \tag{5}$$

with $\exp(x) = e^x$. In this approach, the stress is converging against an ultimate stress σ_{u} with increasing α. The onset of plastic deformation starts at the yield stress σ_{Y} of the material. The exponent p is shaping the stress evolution between σ_{Y} and σ_{u}.

The basic idea is, that plastic flow in the sense of $|\dot{\varepsilon}_{\mathrm{p}}| > 0$ occurs only if a stress state σ_{pr} reaches the current yield limit where $f = 0$. Stress states σ_{pr} for which $f < 0$ are elastic in the Prandtl layer and no change in ε_{p} takes place and thus $\dot{\varepsilon}_{\mathrm{p}} = 0$.

The evolutionary equation for α is simply

$$\dot{\alpha} = |\dot{\varepsilon}_{\mathrm{p}}| \tag{6}$$

The flow rule is defined as

$$\dot{\varepsilon}_{\mathrm{p}} = \gamma \ \mathrm{sign}(\sigma_{\mathrm{pr}}) \tag{7}$$

with the function γ being the slip rate.

The evolutionary equation for the scalar damage variable D is defined in accordance with the exponential hardening law (Eq. (5)) and depends on the history of permanent deformation, (Zysset, 1994; Garcia, 2006; Garcia et al., 2010; Schwiedrzik and Zysset, 2013).

$$D = 1 - \exp(-\alpha p) \tag{8}$$

This leads to a linear evolution of D with the current yield limit. $D = 0$ for the current yield limit being at σ_{Y} and $D = 1$ for the current

yield limit reaching the ultimate stress σ_u and a linear characteristic in between.

Stress σ_{pr} and γ are restricted by the *Kuhn–Tucker complementary conditions*, (Simo and Hughes, 1998): First, σ_{pr} needs to be admissible and reside within or on (but not outside) the yield surface. In addition, plastic flow must go into the direction of the applied stress, which implies γ to be non-negative. Consequently,

$$f(\sigma_{pr}, \alpha) \leq 0 \quad \text{and} \quad \gamma \geq 0 \tag{9}$$

Second, it is required that plastic flow occurs only for stress states residing on the yield surface and that stress states which reside within the yield surface do not lead to plastic flow.

$$\gamma f(\sigma_{pr}, \alpha) = 0 \tag{10}$$

For $\dot{\varepsilon}_p$ being non-zero, the stress point must *persist* on the yield surface so that $\dot{f}(\sigma_{pr}, \alpha) = 0$ for $\gamma > 0$, (Simo and Hughes, 1998). This adds the *persistency* (or *consistency*) condition

$$\gamma \dot{f}(\sigma_{pr}, \alpha) = 0 \quad (\text{if} \quad f(\sigma_{pr}, \alpha) = 0) \tag{11}$$

From the consistency condition (Eq. (11)), it follows that γ can be nonzero only if

$$\dot{f} = \frac{\partial f}{\partial \sigma_{pr}} \dot{\sigma}_{pr} + \frac{\partial f}{\partial \alpha} \dot{\alpha} = 0 \tag{12}$$

From (Eq. (12)), substituting (Eqs. (5), (6), (7)) and with the stress rate being derived from (Eq. (4))

$$\dot{\sigma}_{pr} = \dot{\hat{E}}_{pr}(\varepsilon - \varepsilon_p) + \hat{E}_{pr}(\dot{\varepsilon} - \dot{\varepsilon}_p) \tag{13}$$

together with the rate of modulus change derived from (Eq. (3))

$$\dot{\hat{E}}_{pr} = -\dot{D} E_{pr} = -\dot{\alpha} p \exp(-\alpha p) E_{pr} \tag{14}$$

it is possible to solve for the slip rate γ in case of plastic flow ($f(\sigma_{pr}, \alpha) = 0$). Together with the Kuhn–Tucker condition (Eq. (10)), one obtains the expressions for the slip rate

$$\gamma = \begin{cases} \frac{\operatorname{sign}(\sigma_{pr}) \exp(-p\alpha) E_{pr} \dot{\varepsilon}}{\operatorname{sign}(\sigma_{pr}) p \sigma_{pr} + \exp(-p\alpha) E_{pr} + (\sigma_u - \sigma_Y) p \exp(-p\alpha)}, & \text{if } f(\sigma_{pr}, \alpha) = 0 \\ 0, \quad \text{if } f(\sigma_{pr}, \alpha) < 0 \end{cases} \tag{15}$$

A possible solution strategy for the Prandtl layer is described in Appendix A.

Maxwell layer with variable spring stiffness:. The Maxwell layer is built from an elastic spring in series with a viscous damper with coefficient of viscosity η, Fig. 1. The stiffness of the elastic spring is degrading from its initial value E_{mx} in the amount of damage D resulting in a degraded elastic modulus $\hat{E}_{mx}$ according to

$$\hat{E}_{mx} = (1 - D) E_{mx} \tag{16}$$

The damage variable D is driven by the amount of equivalent plastic strain α in the Prandtl layer by (Eq. (8)). Thus, the degradation of both springs in the 2-layer model is synced and allows – theoretically – for a total vanishing of the model's stress response if $D = 1$. This corresponds to a complete bone material failure.

The stress σ_{mx} and stress rate $\dot{\sigma}_{mx}$ in the Maxwell layer is

$$\begin{aligned} \sigma_{mx} &= \hat{E}_{mx}(\varepsilon - \varepsilon_v) \\ \dot{\sigma}_{mx} &= \dot{\hat{E}}_{mx}(\varepsilon - \varepsilon_v) + \hat{E}_{mx}(\dot{\varepsilon} - \dot{\varepsilon}_v) \end{aligned} \tag{17}$$

With the constitutive law of the damper,

$$\dot{\varepsilon}_v = \frac{\sigma_{mx}}{\eta} \tag{18}$$

one obtains from (Eq. (17)) the governing differential equation for the Maxwell layer

$$\dot{\sigma}_{mx} = \hat{E}_{mx} \dot{\varepsilon} + \frac{\sigma_{mx} \dot{\hat{E}}_{mx}}{\hat{E}_{mx}} - \frac{\hat{E}_{mx}}{\eta} \sigma_{mx} \tag{19}$$

As material properties change here over time, this version of the Maxwell layer is *not* linear-viscoelastic, as opposed to the classic Maxwell model, described e.g. in Marques and Creus (2012).

Time integration:. For a *strain driven process*, ε (and thus $\dot{\varepsilon}$) is a known time signal over time t. Then, the problem to be solved consists of determining the stress response in the Prandtl layer σ_{pr} and the Maxwell layer σ_{mx} and adding them up to the total model stress σ_{mod} according to Eq. (1). Due to the topology of the model and the usage of the damage variable D, σ_{pr} and σ_{mx} are *weakly* coupled. Both layers can be solved separately, but a specific order is required. The solution of σ_{pr} is to be done first as to generate the time history of the damage variable D which is then used as an input for the solution of the Maxwell layer stress response σ_{mx}.

Time integration strategies for the Prandtl layer were adapted from Reisinger et al. (2020) and are described in Appendix A. As the Maxwell layer with degrading stiffness is non-linear-viscoelastic due to its changing material properties over time, it cannot be solved with the hereditary integral, (Gutierrez-Lemini, 2014). Its solution needs to be obtained by solving the ODE, (Eq. (19)). This can be done by standard ODE solvers. In this study, (Eq. (19)) was solved efficiently using an implicit Euler algorithm, as described in Appendix B.

DMA properties:. For comparison of the pure visco-elastic properties of the 2-layer model with Dynamic Mechanical Analysis (DMA) data from other studies, its storage modulus E', loss modulus E'' and loss tangent $\tan(\delta)$ can be derived. This was already laid out in detail in Reisinger et al. (2020) and is summarized here.

In short, for a harmonic excitation, the 2-layer elasto-visco-plastic model from Fig. 1 behaves like a Zener model if operated in the elastic range. With the constants

$$\begin{aligned} a &= \frac{\eta}{E_{mx}} \\ b &= E_{pr} \\ c &= \frac{\eta (E_{pr} + E_{mx})}{E_{mx}} \end{aligned} \tag{20}$$

the frequency dependent *complex modulus* E^* is found to be

$$E^*(\omega) = E'(\omega) + i E''(\omega) = \frac{ac\omega^2 + b}{a^2\omega^2 + 1} + i \frac{c\omega - ab\omega}{a^2\omega^2 + 1} \tag{21}$$

From Eq. (21), the storage modulus E' and loss modulus E'' can be easily extracted for a given angular frequency ω. The *loss tangent* (or *loss factor*) is the tangent of the phase shift δ between strain excitation and stress response and given by

$$\tan(\delta) = \frac{E''}{E'} = \frac{c\omega - ab\omega}{ac\omega^2 + b} \tag{22}$$

Long-term and instantaneous Young's modulus:. When loading the 2-layer model quasi-statically, the Maxwell layer has no stress contribution and stays fully relaxed ($\sigma_{mx} = 0$). Similarly, holding a certain deformation state until the viscous stress contribution is decayed also results in $\sigma_{mx} = 0$. In these two cases, the model stiffness is solely driven by the elastic spring in the Prandtl layer. E_{pr} can be therefore referred to as the *quasi-static* or *long term* Young's modulus of the model if operated in its elastic range.

In contrast, when applying a step load on the model in the form of a Heaviside step function, the apparent model stiffness is the sum $E_{pr} + E_{mx}$, which is therefore referred to as the *instantaneous* Young's modulus.

So E_{pr} and $E_{pr} + E_{mx}$ make up the lower and the upper bound in between any apparent Young's modulus obtained at a finite strain rate must reside.

If damage occurs, and thus $D > 0$, the model stiffness degrades accordingly into $\hat{E}_{pr}$ and $\hat{E}_{mx}$ depending on the load history, leading to an altered long term and instantaneous modulus of $\hat{E}_{pr}$ and $\hat{E}_{pr} + \hat{E}_{mx}$, respectively, in the post-yield regime.

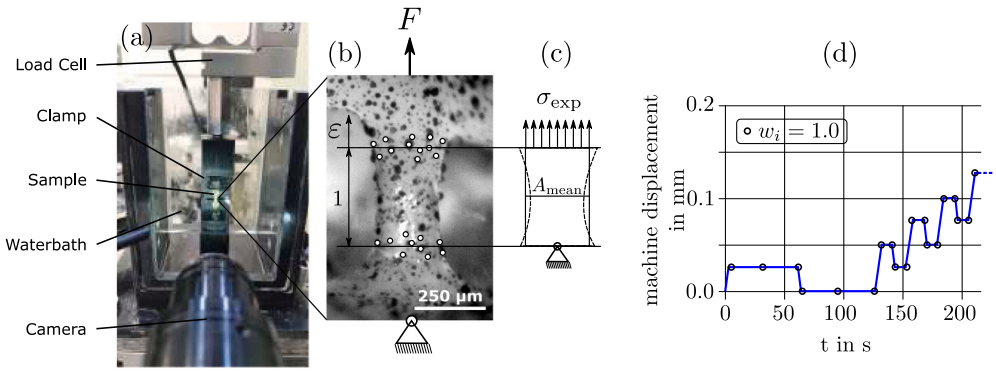

Fig. 2. (a) Tensile test setup with embedded tensile sample. (b) Trabecula, with applied speckle pattern and tracking points at the top and bottom during tensile testing. Horizontal lines indicate the mean vertical position of the points and are used for strain calculation. (c) The representative cross-section A_{mean} of each sample, determined from μCT scans, is used for stress calculation. (d) Loading profile of the trabecular sample with controlled machine displacement over time. The white circles indicate points at which the RMSE objective function is weighted with weighting factor $w_i = 1.0$. $w_i = 0.0$ otherwise. The apparent Young's modulus E_{app} is extracted from the stress–strain data of the first loading ramp.

2.2. Tensile testing of individual trabeculae

In Reisinger et al. (2020), the 2-layer elasto-visco-plastic rheological model was validated against a set of micro-tensile test data of individual bone trabeculae in wet condition to demonstrate its capabilities. As the current study aims to investigate the implications of extending the model by a damage law, the exact same set of mechanical test data is used as in. In the following, the experiments are briefly recapitulated. For more details, refer also to Frank et al. (2018).

Sample preparation:. The usage of human tissue in this study was approved by the Southampton and SouthWest Hampshire Research Ethics Committee, ethic votes LREC 194/99/1, 210/01, 12/SC/0325. Individual trabeculae were dissected from the central femoral head of a 61 year old female donor.

The geometry of every trabeculae was obtained with a calibrated μCT100 (Scanco Medical AG, Switzerland) at 70 kVp, 114 μA, integration time 200 ms, average data 4, 1500 projections, nominal resolution of 3.3 µm and aluminum filter 0.5 mm.

Mechanical testing:. Individual samples were mounted to a servo-electric load-frame (SELmini-001, Thelkin AG, Switzerland), equipped with a custom made tensile test set-up, Fig. 2(a), (Frank et al., 2018).

The whole set-up is placed in a water bath, which is filled with Hank's Balanced Salt Solution (HBSS) to mimic a physiologic environment.

Strain determination is performed by digital image correlation (DIC). The change in distance between points at the sample top and bottom, related to their original distance, yields the engineering strain ε, Fig. 2(b).

A 10 N load cell (HBM-S2M, Germany) was used to measure the experimental force. A representative cross-sectional area A_{mean} was then determined by dividing the obtained volume of each trabeculae (from the μCT, as presented in Frank et al. (2017)) by its length. With this, engineering stress was calculated by $\sigma_{\text{exp}} = F/A_{\text{mean}}$, where F is the force signal, Fig. 2(c).

Loading profile:. A preload of ~0.05N was applied and held for 30 s to align parts and close gaps within the clamps. The main loading profile was displacement-controlled and attempted to accentuate the viscous and plastic response of the sample, Fig. 2(d). In each cycle, an additional displacement of 0.05 mm was applied, compared to the previous step, and held for 10 s. Then, it was unloaded by 0.025 mm and held for 10 s. This procedure of loading, holding, unloading, holding continued until the sample was fractured. The obtained measurement data was resampled to 1 Hz, which appeared to be a good balance between reducing the computational expense for solving the model and integration accuracy.

The samples fractured at different points in time. To unify the data, the time series were cut off at the end of the loading phase of the 5th loading cycle. Samples that fractured before that, were excluded from the study. As the time series is used as an input for the 2-layer model, the preload had to be excluded from the data by shifting load and displacement to be 0.0 at $t = 0$. That was necessary to avoid a step load as model input, that would lead to an unrealistic initial viscous stress response. After optimization, σ_{Y} and σ_{u} were then corrected for the prestress originating from the applied preload.

Due to the delicate nature of the experiment, 13 out of 28 samples had to be removed from the study. In particular, seven samples suffered from difficulties during testing, two samples fractured too early along the load protocol and four samples showed severe discrepancies between stress and strain signals, that became visible during data processing. Finally, fifteen ($n = 15$) samples went successfully through the above experimental procedure and were included in the study.

2.3. Material parameter identification:

A set of material parameters $\underline{q} = [E_{\text{pr}}, \sigma_{\text{Y}}, \sigma_{\text{u}}, p, E_{\text{mx}}, \eta]$ shall now be found, for which the stress response of the 2-layer model σ_{mod} fits best to the measured stress response σ_{exp} of a trabecular sample. This is achieved by an optimization process that is identical to the one in Reisinger et al. (2020). To ease further understanding, the most important steps are repeated here.

The goodness of fit between σ_{mod} and σ_{exp} is expressed in terms of the *root mean square error* (RMSE_{w}) evaluated at all time points t_i of the time series, (Chai and Draxler, 2014; Crawley, 2007).

$$\text{RMSE}(\underline{q}) = \sqrt{\frac{1}{n}\sum_{i=1}^{n}(\sigma_{\text{mod}}(\underline{q}, \varepsilon, t_i) - \sigma_{\text{exp}}(t_i))^2} \tag{23}$$

A weighting factor w_i is introduced that enables to emphasize certain time points in the optimization process leading to the *weighted RMSE*.

$$\text{RMSE}_{\text{w}}(\underline{q}) = \sqrt{\frac{1}{n}\sum_{i=1}^{n} w_i(\sigma_{\text{mod}}(\underline{q}, \varepsilon, t_i) - \sigma_{\text{exp}}(t_i))^2} \tag{24}$$

The optimization process is more robust, when $w_i = 1.0$ at the corner points highlighted in Fig. 2(d) and $w_i = 0.0$ otherwise, (Reisinger et al., 2020; Frank et al., 2021), and thus w_i was set this way.

Eq. (24) is taken as the objective function for the optimization task, which consists of choosing $\underline{q}$ so that

$$\text{RMSE}_{\text{w}}(\underline{q}) \rightarrow \min \quad \text{with} \quad \{\underline{q} \in \mathbb{R} \mid \underline{q} > 0\} \tag{25}$$

Table 1
Table containing the material parameter ranges used for the multi-start optimization method.

q_i	q_{iL}	q_{iR}	Unit
E_{pr}	500	5000	MPa
σ_Y	10	100	MPa
σ_u	σ_Y + 10	σ_Y + 100	MPa
p	10	1000	1
E_{mx}	500	5000	MPa
η	2000	20 000	MPa s

The optimization task from Eq. (25) is addressed with a downhill simplex algorithm, (Nelder and Mead, 1965) performed at 4096 different starting points for $\underline{q}$. In this *multi-start method*, each material parameter q_i in $\underline{q}$ was assigned a meaningful range $q_{iL} \leq q_i \leq q_{iR}$, identical to Reisinger et al. (2020), Table 1. Each range was subdivided by 4 points leading to $4^6 = 4096$ starting points and as much optimization runs. The solution with the minimum $RMSE_w$ value was selected, and considered as quasi 'global' solution. The standard RMSE value according to Eq. (23) was also calculated to ease result interpretation.

In addition to the optimization approach, the Young's modulus of each sample was evaluated classically by a linear fit in the stress–strain curve's first loading cycle, assuming linear elastic behavior. The slope of that regression line is referred to as the apparent Young's modulus E_{app}, (Frank et al., 2018; Reisinger et al., 2020). As the experiments were conducted at a finite strain rate, E_{app} lies in principle somewhere in between the longterm modulus and the instantaneous modulus of the samples.

2.4. Statistics (model comparison)

One goal of this study was to compare the new elasto-visco-plastic 2-layer rheological model with damage law with its predecessor without damage law in terms of their capabilities of reproducing the same micro-tensile experiments on bone tissue. Thus, two groups of result data needed to be compared. For easy referral the following nomenclature was used:

The new model with damage law, as introduced in this manuscript, was denoted as the 'damage model' and in short 'D = on'. The model without damage law from Reisinger et al. (2020) was denoted as the 'non-damage model' or 'D = off'.

For each trabecular sample, the presented material parameter identification procedure lead to a $\underline{q}^{D=on}$ and $RMSE^{D=on}$ that was paired to the corresponding $\underline{q}^{D=off}$ and $RMSE^{D=off}$ value from (Reisinger et al., 2020).

To determine whether the means of that two groups are significantly different, a two-tailed, paired students t-test was applied with a confidence level of 95% ($\alpha = 0.05$). Normality of the data was confirmed by a Kolmogorov–Smirnov test.

3. Results

One sample had to be excluded from the study as no meaningful model fit could be achieved with the damage model, resulting in $n = 14$ valid samples. The damage model could be fit to the tensile test data sets with an average RMSE value of 2.52 ± 1.06 MPa compared to 3.03 ± 1.77 MPa for the non-damage model. The identified material parameters of both models are reported in Table 2 and Fig. 3 and juxtaposed against each other. The listed yield stress σ_Y and ultimate stress σ_u are already corrected for the prestress in each sample.

The found values for E_{pr} and E_{mx} exceed the range of starting values of the optimization procedure, Table 1. This can limit the efficiency of the multistart algorithm as it lowers the probability of finding the global minimum. (To test the detriment of this effect, a small side study was conducted. Hereby, the parameter range of the multistart algorithm was altered to include the final results of Table 2 and the study was then re-evaluated. By doing so, the RMSE dropped slightly from the reported 2.52 ± 1.06 MPa to 2.48 ± 1.09 MPa. However, to stay consistent with the original study of Reisinger et al. (2020) in terms of the applied methodology, this marginal improvement in RMSE of 1.6% was not realized thereafter.)

Table 2
(a) Average material parameters and their standard deviation from $n = 14$ tensile trabecular samples, identified by fitting the 2-layer rheological models to mechanical test data. The asterisk (*) indicates a significant difference ($\alpha = 0.05$) between the model without damage law (D = off) from Reisinger et al. (2020) and the model with damage law (D = on). (σ_Y and σ_u are corrected for the preload.) (b) Apparent Young's modulus as directly extracted from stress–strain curves.

(a)	D = off n = 14 Avg. ± Stdev.	D = on n = 14 Avg. ± Stdev.	Unit	p
RMSE	3.03 ± 1.77	2.52 ± 1.06	MPa	0.119
E_{pr}	3.59 ± 2.09	5.73 ± 3.36	GPa	0.001*
σ_Y	17.81 ± 12.61	19.84 ± 12.43	MPa	0.718
σ_u	60.08 ± 20.08	78.12 ± 26.23	MPa	0.000*
p	177.0 ± 116.7	81.02 ± 69.57	1	0.019*
E_{mx}	1.94 ± 1.02	5.67 ± 6.19	GPa	0.029*
η	2.83 ± 1.03	4.72 ± 2.24	GPa s	0.004*
$E_{pr} + E_{mx}$	5.53 ± 2.73	11.92 ± 8.67	GPa	0.007*
$\tan(\delta)$	0.04 ± 0.03	0.12 ± 0.17	1	0.116
(b)	Avg. ± Stdev.	Avg. ± Stdev.	Unit	
E_{app}	6.32 ± 4.77	6.32 ± 4.77	GPa	

Significant differences between the damage and non-damage model are found for E_{pr}, E_{mx}, σ_u, p and η. In particular, E_{pr}, E_{mx} and η are higher in case of enabled damage law, indicating a generally higher (initial) model stiffness. E_{pr} and E_{mx} reach now the magnitude of the apparent modulus E_{app} of 6.32 ± 4.77 MPa whereas E_{app} falls on the lower side in between the longterm modulus E_{pr} and the instantaneous modulus $E_{pr} + E_{mx}$.

The fit of the damage model to the experimental data resulted in an higher ultimate stress of $\sigma_u = 78.12 \pm 26.23$ MPa compared to the non-damage model. This value is close to the apparent failure stress of the samples of 70.43 ± 26.5 MPa as measured in the experiments. Note: This observed failure stress includes also a viscous stress contribution, whereas σ_u does not.

On average, the RMSE value is lower for the damage model compared to the non-damage model, Table 2. However this is not a significant difference. On the level of individual samples, a better representation of the experimental data by the damage model is observed in the stress–strain data. Fig. 4(a) shows a representative sample with decreasing slope in its hysteresis loops (magenta straight lines). The damage model accounts for this behavior, although the RMSE has not improved much with 5.7 MPa vs. 6.1 MPa. This could be attributed to a high noise in the first loading ramp, as seen in the strain input signal, Appendix C. In Fig. 4(b) the growth of the damage variable D can be observed, which reaches a maximum of around 0.8 at a strain level of 7%.

The trend of D for all samples is shown in Fig. 5. Note, that the last point of each curve corresponds to the middle of the 5th loading cycle where the experimental data was truncated and not to the point of failure. The samples reached different states of damage in the range of ~0.2 to ~0.8 at this point. Fig. 5(b) clearly shows the cyclewise growth of D averaged over all samples and the standard deviation bandwidth.

4. Discussion

In this study, an updated version of the 2-layer elasto-visco-plastic rheological model from Reisinger et al. (2020) is presented that incorporates the effect of damage as degrading model stiffness. The new damage model and older non-damage model are used in an optimization procedure to identify a set of elasto-visco-plastic material

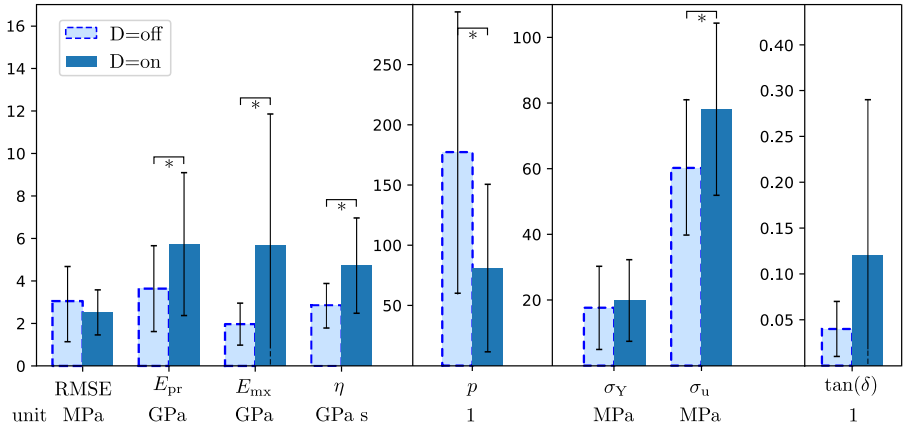

Fig. 3. Average material parameters and their standard deviation from $n = 15$ tensile trabecular samples, identified by fitting the 2-layer rheological models to mechanical test data. The asterisk (*) indicates a significant difference ($\alpha = 0.05$) between the model without damage law (D = off) from Reisinger et al. (2020) and the new model with a damage law (D = on). (σ_Y and σ_u are corrected for the preload.).

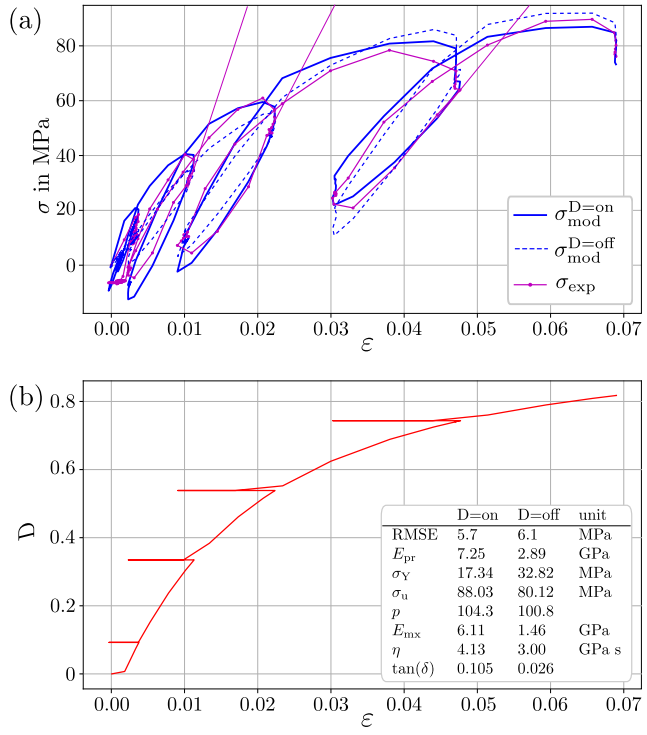

Fig. 4. Selected tensile behavior of a single trabecular sample (id: A2439_T24) as measured experimentally (magenta) vs. simulated by the 2-layer models (blue: with damage law, dashed blue: without damage law). (a) Stress–strain relationship comparing experiments and 2-layer model. Straight lines in magenta indicate the unloading stiffness for each loading cycle. Further data of this sample is depicted in Appendix C. (b) Damage evolution over strain and the identified material parameters for this sample.

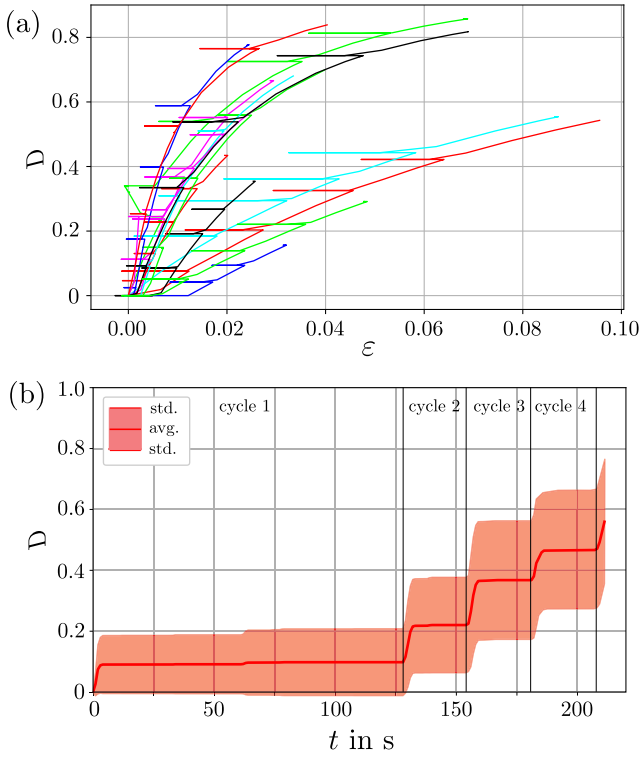

Fig. 5. Damage evolution for all (n = 14) samples. (a) Damage growth of individual samples over strain. The horizontal spikes correspond to the unloading part of the loading cycles. (b) Damage growth over time separated in load cycles. Solid line is the average value, the shaded area correspond to the standard deviation.

properties of trabecular bone tissue from cyclic tensile test data. The performance and obtained material properties are compared and the damage growth is discussed.

Model performance:. Applying the damage model to the tensile test data lead to a slightly better fit, indicated by a lower – albeit not significantly – RMSE value. From this perspective, it cannot be stated that the inclusion of damage in the model better represents the data compared to the non-damage model. However, by investigating individual sample fits, such as in Fig. 4a, it has definitely an advantage in reproducing the obvious apparent stiffness loss in the later course of the loading history. The reason, why no significant improvement in the RMSE values is observed, could be attributed to the already good fit of the non-damage model with an RMSE of 3.03 MPa which is below 5% of the average load amplitude in the experiments. The amount of noise in the experimental data, which is generally high, especially in the first loading ramps at small strains, could prevent a significant reduction in RMSE at all. An example for the signal noise is shown in Appendix C.

Damage:. Unlike previously assumed in Reisinger et al. (2020), the amount of stiffness degradation from damage was high and should not be neglected. Partly very high damage values of D up to ~0.8 for the final load cycle were now found, Fig. 5(a). Stiffness degradation

Table 3
Comparison of modulus reduction with respect to the previous cycle as identified in this study with the damage model vs. a similar study from Frank et al. (2021) with (n=154) were loading and unloading stiffness was evaluated separately.

Cycle	This study	Frank et al. (2021)	
	Damage model	Loading	Unloading
2	−13.5%	+10.2%	−29.3%
3	−17.9%	+11.5%	−23.9%
4	−15.6%	−10.8%	−12.5%

appears to be a significant mechanism during deformation of individual trabeculae.

This is interesting, as compact bone at the microscale shows hardly any damage. Schwiedrzik et al. (2014) tested cylinders of a few microns in diameter in dry condition under cyclic overload compression. There, micropillar tests indicated a high ductility but a very low modulus reduction of only 5% until failure.

On the larger length-scale of the full trabecular network, damage evolves with a mixture of mechanisms. Damage is typically associated with the amount of fractured trabeculae, (Keaveny et al., 1994b; Zysset and Curnier, 1996), but also with microdamage (linear microcracks and/or diffuse damage), (Lambers et al., 2013). The average damage value D at the point of failure for bovine trabecular bone was reported in Zysset and Curnier (1996) to be around 0.55. Lambers et al. (2013) investigated the microdamage in vertebral trabecular bone in compression experiments and reported damage values of 0.6–0.8 at failure. Similar values were observed in the present study. For cortical bone, which is compact and more comparable to individual trabecular tissue, damage values of 0.6 were found by Mirzaali et al. (2015) using also a rheological model framework. The point of failure is not reached in this study as the data was truncated within the 5th loading cycle. A general comparison is still feasible as the 5th cycle was often times already close to sample failure. A good agreement of the current study with the above mentioned literature values can be noted when viewing Fig. 5(b).

For the current study, at the length-scale of single trabeculae, damage is caused by linear microcracks and diffuse damage. Crack size and damage density were shown to increase with plastic strain, (Jungmann et al., 2011; Frank et al., 2018, 2020). The damaged zones are thereby observed as whitening. In a similar but larger study of Frank et al. (2021), an evaluation of the apparent stiffness reduction during identical experiments as in this study was performed. A different and larger set of samples ($n = 154$) was investigated while the experimental protocol and specimen type was exactly the same as in this study. The authors extracted the σ-ε slope in the loading- and unloading phase of each load cycle. The found modulus reduction from cycle to cycle is listed in Table 3 and juxtaposed with the found modulus reduction of this study calculated from the increase in D. It can be seen, that for the loading phase, (Frank et al., 2021) did not observe significant damage, whereas for the unloading phase, higher damage values were reported. The current study fits well into the ranges, supporting the general applicability of the inverse rheological modeling approach to identify damage.

The path at which D is evolving over strain ε varies a lot between the samples, Fig. 5(a). As the growth of D depends on the plastic deformation regime, it relies on the yield point σ_Y, the hardening behavior, determined by p and σ_u, and E_{pr}. All of these parameters have rather high standard deviations, Table 2. This could be attributed to actual variations in the tested bone material, such as trabecular packet size and -number or distribution of mineralization, (Roschger et al., 2008; Ruffoni et al., 2007). However, the samples stem from the same femoral head center where the difference in material composition should be small. It is therefore also possible that experimental uncertainties and different local minima in the optimization procedure contribute to the high standard deviation.

The damage law introduced in this manuscript is solely driven by equivalent plastic strain. This approach does not increase the number of model parameters with respect to the non-damage model from Reisinger et al. (2020). As the challenge of material parameter identification greatly depends on the number of parameters, the numerical expense in the optimization process also remains at the same level and additionally a direct comparison of the obtained material parameters was possible. In other approaches, the accumulation of damage lead to additional parameters, though. Such as in Garcia et al. (2010), where a damage threshold is introduced separately from a yield stress. Similarly, in the viscoplastic model of Fondrk et al. (1999), different values for tensile and compressive dashpot motion were allowed. In comparison, the current approach has a relatively low number of parameters, which is beneficial for material parameter identification purposes.

Bone tissue damage is generally visible as hysteresis loops with decreasing slope from load cycle to load cycle in the post yield regime. This effect was shown experimentally in numerous studies, e.g. Keaveny et al. (1999), Pattin et al. (1996). It is often stated that in each reloading section of a loop, the tangent stiffness appears colinear with the origin — an effect that was reported to be attributed to separate phases of plastic deformation and damage accumulation (Garcia et al., 2010; Keaveny et al., 1994b). Constitutive material models for bone exist, that incorporate that colinearity condition, such as (Garcia et al., 2009, 2010). The data of this study, however, shows elliptical viscous hysteresis cycles that are indistinct with respect to colinearity. The damage model does not require colinearity with the origin and can capture the measured behavior.

Layer elastic moduli:. The usage of the damage model lead to an increase in the identified elastic moduli of both model layers. This is a logical consequence of the apparent modulus reduction in the course of the loading history. The optimizer is logically increasing the model stiffness in order to meet the stress niveau later in the loading history. The increased values of longterm and instantaneous modulus of 5.73 GPa and 11.92 GPa, respectively, are now better supported by values reported in the literature. Apparent stiffness values of other studies ideally reside in this range, as a finite strain rate is neither quasi-static nor infinitely high. Frank et al. (2017, 2018) tested wet bovine trabeculae in two studies in tension and reported an average apparent Young's modulus of 8.2 GPa and 6.5 GPa, respectively. Osteoporotic and non-osteoporotic wet human trabeculae were tested in Frank et al. (2021) and apparent moduli of 7.7 GPa and 8.5 GPa were found for the two groups. Choi et al. (1990) tested moist cortical- and trabecular specimens and found their apparent Young's modulus to be around 4.59 GPa and 5.44 GPa, respectively, which is on the lower side of the current study's results. Other studies are hardly comparable as experiments were conducted mostly under dry sample conditions. For a recent review on individual trabeculae properties, consult (Wu et al., 2018).

Yield stress:. The damage model identified an average yield stress σ_Y of 19.84 MPa. This is a slight increase compared to the non-damage model value of 17.81 MPa but is still low compared to other studies.

Values of 60–80 MPa were found in wet micro-tensile tests on bovine trabeculae, Frank et al. (2017, 2018). Carretta et al. (2013a) reported between 78 MPa and 115 MPa as measured on dry bovine trabeculae and in Carretta et al. (2013b) 115–130 MPa for dry human femoral trabeculae were obtained. Tensile tests on wet compact bone specimens provide a yield limit of 122.3 MPa, (Currey, 2004).

Still valid reasons for this rather large gap is already discussed in Reisinger et al. (2020) and briefy updated here.

The yield limit of bone is often discussed to be rather a yield zone, (Wolfram and Schwiedrzik, 2016) — a stress range in which areas of plastic deformation grow in the material. This concept is contradictory to identify a single yield point in a stress–strain diagram. Nevertheless, different common methods exist to do so, such as using the 0.2% limit of strain or line intersections, (Reilly and Burstein, 1975; Keaveny et al., 1994a). This ambiguity might be one of the reasons

why the model output differs a lot from yield-points extracted from stress–strain data.

In addition, the yield stress σ_Y obtained from the two-layer model is excluding viscous effects and represents a pure quasi-static quantity. From the theoretical point of view, an apparent yield point, extracted directly from force–displacement data, is therefore in general higher, depending on strain rate, (McElhaney, 1966).

Nevertheless, the deviation of the current study's σ_Y from literature values is very large and need to be explained by further investigations.

Viscosity and ultimate properties:. The damping parameter η almost doubled from the non-damage to the damage model output. η contributes to the overall model stiffness and this tendency is in line with the reasons given above for the increase of the elastic moduli. Similarly $\tan(\delta)$ increased threefold from 0.04 to 0.12 for 1 Hz exitation.

The ultimate stress σ_u and hardening parameter p significantly changed when switching from the non-damage model to the damage model, Table 2. σ_u is the theoretical max. stress at which also $D = 1$ and the model stiffness is vanishing, which is a point that is impossible to reach. p shapes the hardening regime. Both parameters are of rather theoretical nature and the interpretation of their value shift remains open at this point.

In the 2-layer model presented here, the one viscous element is activated by elastic and plastic strain. However, there are indications from experiments on different length-scales of bone, that visco-elasticity and visco-plasticity are presumably separate deformation processes that should be treated differently. Other works incorporate that distinction in their models, such as (Zysset, 1994; Schwiedrzik et al., 2014), which in turn leads to additional model parameters.

Limitations:. Identical to Reisinger et al. (2020), the geometrically linear formulation of the model, restricts its usage to small strains only. Second, despite using a multistart approach, it remains unknown whether the global minimum or a local minimum was found in the optimization process.

The damage model was tested for cyclic loading that stays in the tensile regime. For load protocols that produce alternating stress, a more complex damage coupling needs to be considered, as tensile and compressive damage rely on different mechanisms, (Zysset et al., 2016).

A general limitation of the described modeling approach is its phenomenological nature. It is solely reproducing the stress–strain response of bone tissue observed in experiments. Therefore no mechanistic insights into plasticity and damage can be gained.

5. Conclusion

The introduction of the damage law into the 2-layer elasto-visco-plastic rheological model leads to a better consideration of the actual shapes of stress–strain data. Specifically, the post-yield stress–strain response, where clear stiffness degradation is visible in the experiments, can be now closely reproduced. However, the improvement did not reach statistical significance when measured using the RMSE metric.

The effect of damage appears to be a significant mechanism at the level of individual trabeculae as high values were identified after some load cycles, that are in accordance with other literature.

The study suggests, that the proposed inverse modeling approach is a valid tool for evaluating the growth of damage in bone tissue under load.

CRediT authorship contribution statement

Andreas G. Reisinger: Writing – review & editing, Writing – original draft, Visualization, Validation, Software, Resources, Methodology, Investigation, Formal analysis, Conceptualization. **Martin Bittner-Frank:** Writing – original draft, Validation, Methodology, Investigation, Formal analysis, Conceptualization. **Philipp J. Thurner:** Supervision. **Dieter H. Pahr:** Supervision.

Declaration of competing interest

The authors declare that they have no known competing financial interests or personal relationships that could have appeared to influence the work reported in this paper.

Data availability

Data will be made available on request.

Acknowledgments

Full IRB and ethics approvals were obtained for the study (LREC 194/99/1; 210/01; 12/SC/0325) from Southampton and South West Hampshire Research Ethics Committee. The authors thank Prof. Philippe Zysset, University of Bern, for valuable advises with respect to damage modeling of bone.

Appendix A. Solution of the prandtl layer

The problem to be solved in the following, consists of determining the stress in the Prandtl layer σ_{pr} for a given strain signal ε. The following approach was laid out already in Reisinger et al. (2020) for the 2-layer model without damage law. Here, the equations are recapitulated and adapted, allowing for degrading spring stiffnesses according to (Eq. (3)). We sum up the problem in the form of a system of ODEs

$$\underline{\dot{y}}(t) = \underline{g}(t, \underline{y}(t)) \quad \text{with} \quad \underline{y} = \begin{bmatrix} \sigma_{pr} \\ \alpha \end{bmatrix} \tag{26}$$

with $\underline{g}$ being a vector function, comprising of (Eqs. (4), (5), (6), (7), (15)).

The ODE in Eq. (26) is stiff in nature due to the discontinuous Eq. (15). Nevertheless, it can be solved by a standard ODE solver, using e.g. the Backward Differentiation Formula (BDF), (Byrne and Hindmarsh, 1975), and by allowing $f(\sigma_{pr}, \alpha)$ to take 'small' values greater than 0. However, this is highly inefficient.

More favorably, the *return mapping algorithm* for the incremental solution of σ_{pr} is employed, (Simo and Hughes, 1998). Therefore, time and strain are discretized

$$t_{i+1} = t_i + \Delta t \quad \text{and} \quad \varepsilon_{i+1} = \varepsilon_i + \Delta\varepsilon \tag{27}$$

with the time increment Δt and strain increment $\Delta\varepsilon$ advancing time and strain from a state i to the state $i+1$ ($i \in \mathbb{N}$). Solving the problem of Eq. (26) then reduces to finding the model state $\underline{y}_{i+1}$ coming from a known solution $\underline{y}_i$. The new state $\underline{y}_{i+1}$ can be approximated by different integration schemes, from which the *backward (implicit) Euler* algorithm is used for the reason of its unconditional stability, (Hairer et al., 1987). In that framework, the discrete version of Eq. (26) reads

$$\underline{y}_{i+1} = \underline{y}_i + \Delta t\ \underline{g}(t_{i+1}, \underline{y}_{i+1}) \tag{28}$$

The algorithmic counterparts of (Eqs. (4), (5), (6), (7), (8)) are

$$\begin{aligned} \sigma_{pr,i+1} &= (1 - D_{i+1}) E_{pr} (\varepsilon_{i+1} - \varepsilon_{p,i+1}), \\ \varepsilon_{p,i+1} &= \varepsilon_{p,i} + \Delta\gamma\ \operatorname{sign}(\sigma_{pr,i+1}), \\ \alpha_{i+1} &= \alpha_i + \Delta\gamma, \\ f_{i+1} &= |\sigma_{pr,i+1}| - [\sigma_Y + (\sigma_u - \sigma_Y)(1 - \exp(-\alpha_{i+1} p))], \\ D_{i+1} &= 1 - \exp(-\alpha_{i+1} p) \end{aligned} \tag{29}$$

alongside with the discrete version of the Kuhn–Tucker conditions

$$\begin{aligned} f_{i+1} &\le 0, \\ \Delta\gamma &\ge 0, \\ \Delta\gamma\ f_{i+1} &= 0 \end{aligned} \tag{30}$$

where $\Delta\gamma = \gamma_{i+1}\Delta t$ is a Lagrange multiplier.

The return mapping strategy involves conducting an elastic *trial* step while freezing plastic flow, defined by

$$\begin{aligned}
\sigma^{\text{trial}}_{\text{pr},i+1} &= (1-D_{i+1})E_{\text{pr}}(\varepsilon_{i+1}-\varepsilon_{\text{p},i}),\\
\varepsilon^{\text{trial}}_{\text{p},i+1} &= \varepsilon_{\text{p},i},\\
\alpha^{\text{trial}}_{i+1} &= \alpha_i,\\
f^{\text{trial}}_{i+1} &= |\sigma^{\text{trial}}_{\text{pr},i+1}| - [\sigma_{\text{Y}} + (\sigma_{\text{u}}-\sigma_{\text{Y}})(1-\exp(-\alpha^{\text{trial}}_{i+1}p))],\\
D^{\text{trial}}_{i+1} &= D_i
\end{aligned} \tag{31}$$

In case, the trial step is admissible in the sense that $f^{\text{trial}}_{i+1} \leq 0$, the trial step *is* in fact the solution to the problem (Eqs. (29), (30)). This step is called a purely *elastic step* and $\Delta\gamma = 0$, giving

$$\left.\begin{aligned}
\sigma_{\text{pr},i+1} &= \sigma^{\text{trial}}_{\text{pr},i+1},\\
\varepsilon_{\text{p},i+1} &= \varepsilon^{\text{trial}}_{\text{p},i+1},\\
\alpha_{i+1} &= \alpha^{\text{trial}}_{i+1},\\
f_{i+1} &= f^{\text{trial}}_{i+1},\\
D_{i+1} &= D^{\text{trial}}_{i+1}
\end{aligned}\right\} \text{if } f^{\text{trial}}_{i+1} \leq 0 \tag{32}$$

In the other case, where the trial step resides outside the yield surface (indicated by $f^{\text{trial}}_{i+1} > 0$) the step under consideration is not admissible in the sense of Eq. (30). The solution to this *plastic step* needs to be obtained by 'correcting' the trial step by

$$\left.\begin{aligned}
\sigma_{\text{pr},i+1} &= (1-D_{i+1})E_{\text{pr}}(\varepsilon_{i+1}-\varepsilon_{\text{p},i}-\Delta\gamma\ \text{sign}(\sigma^{\text{trial}}_{\text{pr},i+1})),\\
\varepsilon_{\text{p},i+1} &= \varepsilon^{\text{trial}}_{\text{p},i+1} + \Delta\gamma\ \text{sign}(\sigma^{\text{trial}}_{\text{pr},i+1}),\\
\alpha_{i+1} &= \alpha^{\text{trial}}_{i+1} + \Delta\gamma,\\
f_{i+1} &\equiv 0,\\
D_{i+1} &= 1-\exp(-(\alpha^{\text{trial}}_{i+1}+\Delta\gamma)p)
\end{aligned}\right\} \text{if } f^{\text{trial}}_{i+1} > 0 \tag{33}$$

Finally, breaking down the requirement $f_{i+1} \equiv 0$ gives the implicit relationship

$$f_{i+1} = |\sigma_{\text{pr},i+1}| - [\sigma_{\text{Y}} + (\sigma_{\text{u}}-\sigma_{\text{Y}})(1-\exp(-p(\alpha_i+\Delta\gamma)))] \equiv 0 \tag{34}$$

or, in short, with Eq. (5)

$$f(\sigma_{\text{pr},i+1}, \alpha_i + \Delta\gamma) = 0 \tag{35}$$

from which the only remaining unknown $\Delta\gamma > 0$ can be obtained numerically via e.g. the Newton–Raphson algorithm.

Appendix B. Solution of the Maxwell layer with variable spring stiffness

The problem to be solved in the following, consists of determining the stress in the Maxwell layer σ_{mx} in the special case of variable spring stiffness. The given signals over time are strain ε and $\hat{E}_{\text{mx}}$, with $\hat{E}_{\text{mx}}$ calculated by (Eq. (16)) using the damage signal $D(t)$, which is an output of the Prandtl layer solution. The ODE has the form

$$\dot{\sigma}_{\text{mx}} = g(t, \sigma_{\text{mx}}) \tag{36}$$

which can be solved by a standard ODE solver. g is a function, containing the right side of (Eq. (19)). However, it turned out, that the standard iterative ODE solver algorithms are too slow, to allow for the large number of solution repetitions needed in this study. Therefore, the problem was solved based on its implicit Euler formulation,

$$\sigma_{\text{mx},i+1} = \sigma_{\text{mx},i} + \Delta t\ g(t_{i+1}, \sigma_{\text{mx},i+1}) \tag{37}$$

with the time incrementation

$$\begin{aligned}
t_{i+1} &= t_i + \Delta t\\
\varepsilon_{i+1} &= \varepsilon_i + \Delta\varepsilon\\
\hat{E}_{\text{mx},i+1} &= \hat{E}_{\text{mx},i} + \Delta\hat{E}_{\text{mx}}
\end{aligned} \tag{38}$$

using the time increment Δt and the state index variable i, ($i \in \mathbb{N}$). It turns out, that, although the general formulation of (Eq. (37)) is implicit, $\sigma_{\text{mx},i+1}$ can be calculated explicitly, leading to a large computational performance gain.

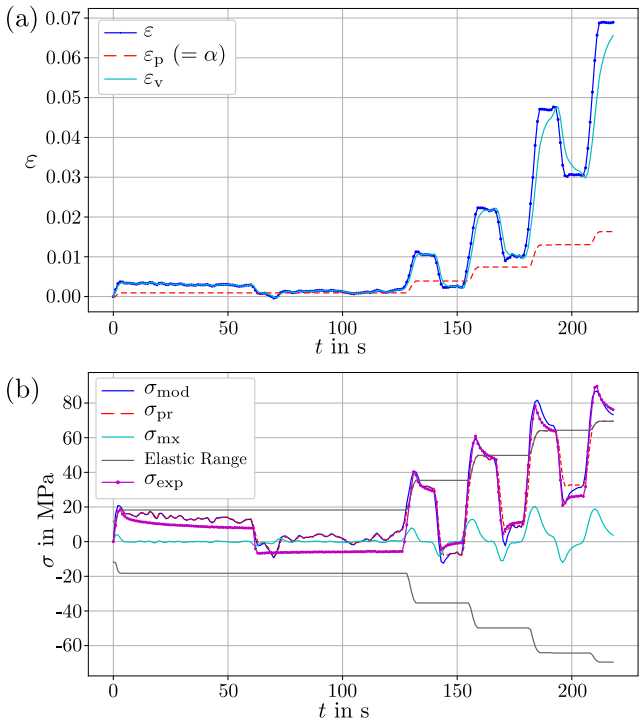

Fig. 6. Selected tensile behavior of the trabecular sample (id: A2439_T24) from Fig. 4 as measured experimentally and as modeled with the damage model. (a) Strain–time signal with total strain ε, plastic strain ε_{p}, viscous strain ε_{v}. (b) Stress–time signal of the experiment σ_{exp} vs. damage model σ_{mod}, including the layer stresses σ_{pr} and σ_{mx}.

After rearranging (Eq. (37)) using (Eqs. (19) and (38)) the explicit expression of $\sigma_{\text{mx},i+1}$ is obtained, which is based only on the solution at stage i and known inputs.

$$\sigma_{\text{mx},i+1} = \frac{\sigma_{\text{mx},i} + \Delta t\ B}{1 - \Delta t\ A} \tag{39}$$

with

$$\begin{aligned}
A &= \frac{\dot{\hat{E}}_{\text{mx},i+1}}{\hat{E}_{\text{mx},i+1}} - \frac{\hat{E}_{\text{mx},i+1}}{\eta}\\
B &= \dot{\varepsilon}_{i+1}\ \hat{E}_{\text{mx},i+1}
\end{aligned} \tag{40}$$

The time step Δt needs to be chosen that a sufficient solution accuracy is maintained. In this study, Δt was set to keep the error below approx. 1% to the exact solution, based on some pretests.

Appendix C. Time signal data of the exemplary sample A2439_T24

Further expanding the details on sample A2439_T24 from (Fig. 4), its strain and stress signals are depicted over time in (Fig. 6). It is clearly seen that especially the first loading cycle is subjected to high noise in the strain signal attributed to the limits of the optical DIC measurement. The corresponding stress signal is clean. Despite this discrepancy in the experiment's stress and strain signal, the model achieved a good fit with an RMSE value of 5.7 MPa.

References

Byrne, G.D., Hindmarsh, A.C., 1975. A polyalgorithm for the numerical solution of ordinary differential equations. ACM Trans. Math. Softw. 1 (1), 71–96.

Carretta, R., Luisier, B., Bernoulli, D., Stüssi, E., Müller, R., Lorenzetti, S., 2013a. Novel method to analyze post-yield mechanical properties at trabecular bone tissue level. J. Mech. Behav. Biomed. Mater. 20, 6–18.

Carretta, R., Stüssi, E., Müller, R., Lorenzetti, S., 2013b. Within subject heterogeneity in tissue-level post-yield mechanical and material properties in human trabecular bone. J. Mech. Behav. Biomed. Mater. 24, 64–73.

Carter, D.R., Hayes, W.C., 1977a. Compact bone fatigue damage: A microscopic examination. Clin. Orthopaed. Relat. Res. (127), 265–274.

Carter, D.R., Hayes, W.C., 1977b. The compressive behavior of bone as a two-phase porous structure. J. Bone Joint Surg. Am. Vol. 59 (7), 954–962.

Chai, T., Draxler, R.R., 2014. Root mean square error (RMSE) or mean absolute error (MAE)?–Arguments against avoiding RMSE in the literature. Geosci. Model Dev. 7 (3), 1247–1250.

Choi, K., Kuhn, J.L., Ciarelli, M.J., Goldstein, S.A., 1990. The elastic moduli of human subchondral, trabecular, and cortical bone tissue and the size-dependency of cortical bone modulus. J. Biomech. 23 (11), 1103–1113.

Crawley, M., 2007. The R Book, first ed. John Wiley & Sons.

Currey, J., 2004. Tensile yield in compact bone is determined by strain, post-yield behaviour by mineral content. J. Biomech. 37 (4), 549–556, URL http://www.sciencedirect.com/science/article/B6T82-49PYKYM-3/2/330ce16337859691d4daa605943891fe.

Fondrk, M.T., Bahniuk, E.H., Davy, D.T., 1999. A damage model for nonlinear tensile behavior of cortical bone. J. Biomech. Eng. 121 (5), 533–541. http://dx.doi.org/10.1115/1.2835084.

Fondrk, M., Bahniuk, E., Davy, D., Michaels, C., 1988. Some viscoplastic characteristics of bovine and human cortical bone. J. Biomech. 21 (8), 623–630. http://dx.doi.org/10.1016/0021-9290(88)90200-X, URL http://www.sciencedirect.com/science/article/pii/002192908890200X.

Frank, M., Fischer, J.T., Thurner, P., 2020. Microdamage formation in individual bovine trabeculae during fatigue testing. J. Biomech. 115, http://dx.doi.org/10.1016/j.jbiomech.2020.110131.

Frank, M., Marx, D., Nedelkovski, V., Pahr, D.H., Thurner, P.J., et al., 2018. Dehydration of individual bovine trabeculae causes transition from ductile to quasi-brittle failure mode. J. Mech. Behav. Biomed. Mater. 87, 296–305.

Frank, M., Marx, D., Pahr, D.H., Thurner, P.J., 2017. Mechanical properties of individual trabeculae in a physiological environment. In: Biomedical Engineering (BioMed), 2017 13th IASTED International Conference on. IEEE, pp. 141–146.

Frank, M., Reisinger, A., Pahr, D., Thurner, P., 2021. Effects of osteoporosis on bone morphometry and material properties of individual human trabeculae in the femoral head. JBMR Plus 5, http://dx.doi.org/10.1002/jbm4.10503.

Garcia, 2006. Elastic Plastic Damage Laws for Cortical Bone (Ph.D. thesis). École polytechnique fédérale de Lausanne.

Garcia, D., Zysset, P., Charlebois, M., Curnier, A., 2009. A three-dimensional elastic plastic damage constitutive law for bone tissue. Biomech. Model. Mechanobiol. 8, 149–165. http://dx.doi.org/10.1007/s10237-008-0125-2.

Garcia, D., Zysset, P.K., Charlebois, M., Curnier, A., 2010. A 1d elastic plastic damage constitutive law for bone tissue. Arch. Appl. Mech. 80 (5), 543–555.

Gelin, J., Ghouati, O., 1995. An inverse method for material parameters estimation in the inelastic range. Comput. Mech. 16 (3), 143–150.

Grzesikiewicz, W., Zbiciak, A., 2012. Study of generalized prandtl rheological model for constitutive description of elastoplastic properties of materials. J. Achiev. Mater. Manuf. Eng. 55 (2), 501–510.

Gutierrez-Lemini, D., 2014. Engineering Viscoelasticity. Springer.

Hairer, E., Norsett, S., Wanner, G., 1987. Solving ordinary differential equations. Part 1.

Ichikawa, Y., Ohkami, T., 1992. A parameter identification procedure as a dual boundary control problem for linear elastic materials. Soils Found. 32 (2), 35–44.

Jungmann, R., Szabo, M., Schitter, G., Tang, RY.S., Vashishth, D., Hansma, P., Thurner, P., 2011. Local strain and damage mapping in single trabeculae during three-point bending tests. J. Mech. Behav. Biomed. Mater. 4 (4), 523–534.

Keaveny, T.M., Wachtel, E.F., Ford, C.M., Hayes, W.C., 1994a. Differences between the tensile and compressive strengths of bovine tibial trabecular bone depend on modulus. J. Biomech. 27 (9), 1137–1146. http://dx.doi.org/10.1016/0021-9290(94)90054-X, URL http://www.sciencedirect.com/science/article/pii/002192909490054X.

Keaveny, T.M., Wachtel, E.F., Guo, X.E., Hayes, W.C., 1994b. Mechanical behavior of damaged trabecular bone. J. Biomech. 27 (11), 1309–1318.

Keaveny, T.M., Wachtel, E.F., Zadesky, S.P., Arramon, Y.P., 1999. Application of the Tsai-Wu quadratic multiaxial failure criterion to bovine trabecular bone. J. Biomech. Eng. 121 (1), 99–107. http://dx.doi.org/10.1115/1.2798051.

Lakes, R.S., Katz, J.L., Sternstein, S.S., 1979. Viscoelastic properties of wet cortical bone—I. Torsional and biaxial studies. J. Biomech. 12 (9), 657–678.

Lambers, F., Bouman, A., Rimnac, C., Hernandez, C., 2013. Microdamage caused by fatigue loading in human cancellous bone: Relationship to reductions in bone biomechanical performance. PLoS One 8, e83662. http://dx.doi.org/10.1371/journal.pone.0083662.

Marques, S.P., Creus, G.J., 2012. Computational Viscoelasticity. Springer Science & Business Media.

McElhaney, J.H., 1966. Dynamic response of bone and muscle tissue. J. Appl. Physiol. 21 (4), 1231–1236.

Mirzaali, M.J., Bärki, A., Schwiedrzik, J., Zysset, P., Wolfram, U., 2015. Continuum damage interactions between tension and compression in osteonal bone. J. Mech. Behav. Biomed. Mater. 49, http://dx.doi.org/10.1016/j.jmbbm.2015.05.007.

Muller, D., Hartmann, G., 1989. Identification of materials parameters for inelastic constitutive models using principles of biologic evolution. J. Eng. Mater. Technol. 111 (3), 299–305.

Nalla, R.K., Kinney, J.H., Ritchie, R.O., 2003. Mechanistic fracture criteria for the failure of human cortical bone. Nat. Mater. 2 (3), 164–168.

Natali, A.N., Carniel, E.L., Pavan, P.G., 2008. Constitutive modelling of inelastic behaviour of cortical bone. Med. Eng. Phys. 30 (7), 905–912.

Nelder, J.A., Mead, R., 1965. A simplex method for function minimization. Comput. J. 7 (4), 308–313.

Pattin, C., Caler, W., Carter, D., 1996. Cyclic mechanical property degradation during fatigue loading of cortical bone. J. Biomech. 29 (1), 69–79.

Reilly, D.T., Burstein, A.H., 1975. The elastic and ultimate properties of compact bone tissue. J. Biomech. 8 (6), 393–405.

Reilly, D.T., Burstein, A.H., Frankel, V.H., 1974. The elastic modulus for bone. J. Biomech. 7 (3), 271–275. http://dx.doi.org/10.1016/0021-9290(74)90018-9, URL http://www.sciencedirect.com/science/article/pii/0021929074900189.

Reisinger, A.G., Frank, M., Thurner, P.J., Pahr, D.H., 2020. A two-layer elasto-visco-plastic rheological model for the material parameter identification of bone tissue. Biomech. Model. Mechanobiol. http://dx.doi.org/10.1007/s10237-020-01329-0.

Roschger, P., Paschalis, E., Fratzl, P., Klaushofer, K., 2008. Bone mineralization density distribution in health and disease. Bone 42 (3), 456–466. http://dx.doi.org/10.1016/j.bone.2007.10.021, URL http://www.sciencedirect.com/science/article/B6T4Y-4R41K8G-1/2/1e7503a06a93304d3b618b517d4cba6a.

Ruffoni, D., Fratzl, P., Roschger, P., Klaushofer, K., Weinkamer, R., 2007. The bone mineralization density distribution as a fingerprint of the mineralization process. Bone 40 (5), 1308–1319, URL http://www.sciencedirect.com/science/article/pii/S8756328207000373.

Sasaki, N., Nakayama, Y., Yoshikawa, M., Enyo, A., 1993. Stress relaxation function of bone and bone collagen. J. Biomech. 26 (12), 1369–1376.

Schwiedrzik, J.J., 2014. Experimental, theoretical and numerical investigation of the nonlinear micromechanical properties of bone.

Schwiedrzik, J., Raghavan, R., Bürki, A., LeNader, V., Wolfram, U., Michler, J., Zysset, P., 2014. In situ micropillar compression reveals superior strength and ductility but an absence of damage in lamellar bone. Nature Mater. 13 (740).

Schwiedrzik, J., Zysset, P., 2013. An anisotropic elastic-viscoplastic damage model for bone tissue. Biomech. Model. Mechanobiol. 12, 201–213. http://dx.doi.org/10.1007/s10237-012-0392-9.

Simo, J., Hughes, T., 1998. Computational Inelasticity, Vol. 7. Springer-Verlag, New York.

Sperry, W.C., 1964. Rheological-model concept. J. Acoust. Soc. Am. 36 (2), 376–385.

Synek, A., Chevalier, Y., Baumbach, S.F., Pahr, D.H., 2015. The influence of bone density and anisotropy in finite element models of distal radius fracture osteosynthesis: Evaluations and comparison to experiments. J. Biomech. 48 (15), 4116–4123.

Szabó, M., Taylor, M., Thurner, P., 2011. Mechanical properties of single bovine trabeculae are unaffected by strain rate. J. Biomech. 44 (5), 962–967. http://dx.doi.org/10.1016/j.jbiomech.2010.12.008, URL http://www.sciencedirect.com/science/article/pii/S0021929010006962.

Thurner, P., Erickson, B., Jungmann, R., Schriock, Z., Weaver, J., Fantner, G., Schitter, G., Morse, D., Hansma, P., 2007. High-speed photography of compressed human trabecular bone correlates whitening to microscopic damage. Eng. Fract. Mech. 74 (12), 1928–1941. http://dx.doi.org/10.1016/j.engfracmech.2006.05.024, URL http://www.sciencedirect.com/science/article/pii/S0013794406002128, first International Conference on the Mechanics of Biomaterials and Tissues.

Vashishth, D., Tanner, K.E., Bonfield, W., 2000. Contribution, development and morphology of microcracking in cortical bone during crack propagation. J. Biomech. 33 (9), 1169–1174. http://dx.doi.org/10.1016/S0021-9290(00)00010-5, URL http://www.sciencedirect.com/science/article/B6T82-40GHY88-K/2/b54129b23887ba1486b5796137651a16.

Voce, E., 1948. The relationship between stress and strain for homogeneous deformation. J. Inst. Met. 74, 537–562.

Wolfram, U., Schwiedrzik, J., 2016. Post-yield and failure properties of cortical bone. BoneKEy Reports 5, 829. http://dx.doi.org/10.1038/bonekey.2016.60.

Wu, D., Isaksson, P., Ferguson, S.J., Persson, C., 2018. Young's modulus of trabecular bone at the tissue level: A review. Acta Biomater. 78, 1–12. http://dx.doi.org/10.1016/j.actbio.2018.08.001.

Zioupos, P., 1999. On microcracks, microcracking, in-vivo, in vitro, in-situ and other issues.

Zioupos, P., Currey, J., 1994. The extent of microcracking and the morphology of microcracks in damaged bone. J. Mater. Sci. 29 (4), 978–986.

Zysset, P., 1994. A constitutive law for trabecular bone.

Zysset, P., Curnier, A., 1996. A 3D damage model for trabecular bone based on fabric tensors. J. Biomech. 29 (12), 1549–1558. http://dx.doi.org/10.1016/S0021-9290(96)80006-6, URL http://www.sciencedirect.com/science/article/pii/S0021929096800066.

Zysset, P.K., Schwiedrzik, J., Wolfram, U., 2016. European society of biomechanics S.m. Perren award 2016: A statistical damage model for bone tissue based on distinct compressive and tensile cracks. J. Biomech. 49 (15), 3616–3625. http://dx.doi.org/10.1016/j.jbiomech.2016.09.045, URL https://www.sciencedirect.com/science/article/pii/S0021929016311034.